Title: The junctions connecting the endoplasmic reticulum to the nuclear envelope are constricted and remodelled during the cell cycle

Authors: Helena Bragulat-Teixidor[1,2]*, Keisuke Ishihara[3], Gréta Martina Szücs[1], Shotaro Otsuka[1]*

[1]Max Perutz Labs, a joint venture of the University of Vienna and the Medical University of Vienna, Vienna Biocenter, Vienna, Austria.

[2]Vienna BioCenter PhD Program, Doctoral School of the University of Vienna and Medical University of Vienna, Vienna, Austria.

[3]Department of Computational and Systems Biology, School of Medicine, University of Pittsburgh, Pittsburgh, PA, USA.

*Correspondence:

helena.bragulatteixidor@meduniwien.ac.at; shotaro.otsuka@univie.ac.at

Abstract

The endoplasmic reticulum (ER) is physically connected to the cell nucleus via junctions with the nuclear envelope (NE). These ER-NE junctions are essential for supplying the NE with lipids and transmembrane proteins that are synthesized in the ER. Despite the important role of ER-NE junctions, their biogenesis, architecture and maintenance across the cell cycle has remained elusive. In this study, by combining live cell imaging with quantitative three-dimensional electron microscopy, we systematically elucidated the ultrastructure of ER-NE junctions in mammalian cells. We discovered that ER-NE junctions exhibit a constricted hourglass shape that is different from the junctions within the ER. When ER-NE junctions are newly built during NE assembly at mitotic exit, their morphology resembles ER-ER junctions, but they become constricted starting in telophase. Altogether, our findings imply novel mechanisms that remodel ER-NE junctions and have functional implications for the lipid and protein traffic that are crucial for nuclear function.

INTRODUCTION

The endoplasmic reticulum (ER) is the largest membrane-bound organelle in the cell, and the major site of lipid and membrane protein synthesis. The ER makes extensive contacts with other organelles such as mitochondria, the Golgi apparatus, and endosomes. These contact sites play essential roles in protein homeostasis, lipid transfer, metabolite shuffling, ion exchange, and signal transduction (Rossini et al., 2021). In contrast to these "contact sites" at which the ER membranes are tethered to, but not fused with the membranes of other organelles, the ER is linked to the nucleus via direct fusion to the outer nuclear membrane (ONM) of the nuclear envelope (NE) (Friedman and Voeltz, 2011). ER-NE junctions are essential for supplying the lipids and transmembrane proteins that are synthesized in the ER to the NE. The NE proteins supplied via ER-NE junctions play important roles in regulating gene expression, genome organization, lipid metabolism, the formation of nuclear pore complexes, mechanosignalling between the cytoskeleton and the nuclear lamina, nuclear shape and positioning (Gauthier and Comaills, 2021). Hence, nuclear function and morphology depend on a proper communication via ER-NE junctions.

While ER-NE junctions have been discovered more than 60 years ago (Watson, 1955), their precise structure remains elusive. Typically, ER-NE junctions are illustrated in the same way as junctions within the ER, or ER-ER junctions. This view is based on electron microscopy (EM) studies carried out in yeast, and chemically-fixed mammalian, and plant cells, where the morphology of ER-NE and ER-ER junctions are comparable (Watson, 1955; Whaley et al., 1960; Friedman and Voeltz, 2011). However, it has been observed that ER-NE junctions in plant root tip cells are constricted (25-30 nm in diameter) when the samples were high-pressure frozen, but not when they were chemically-fixed (Craig and Staehelin 1988; Staehelin, 1997). Further, there has been no

study that addresses how ER-NE junctions are established and maintained throughout the cell cycle, when the NE breaks down and reforms from the mitotic ER in open mitosis.

In this study, we combined live imaging, high-pressure freezing, and quantitative three-dimensional (3D) EM to systematically study the ultrastructure of ER-NE junctions in mammalian cells in their native state. Strikingly, we discovered that ER-NE junctions have a constricted ultrastructure that is morphologically distinct from the junctions within the ER. By correlating live imaging with electron tomography, we found that the ultrastructure of the ER-NE junctions is remodelled during the cell cycle, and that the morphological specialization of ER-NE junctions starts at telophase. These findings suggest that ER-NE junctions are regulated via a novel mechanism distinct from the one remodelling junctions within the ER. Moreover, the constricted shape of ER-NE junctions has implications on their functional roles in regulation of lipid and protein traffic that are crucial for nuclear function.

RESULTS

Systematic electron microscopy assay for studying ER-NE junctions at different cell cycle stages

To investigate the ultrastructure and abundance of ER-NE junctions during the cell cycle with high temporal resolution, we developed a sequential workflow that combines live cell imaging with high-resolution 3D EM (Figure 1). Cell cycle progression of synchronized HeLa cells was monitored by live cell imaging. When the cells at anaphase and telophase were enriched, they were rapidly immobilized by high-pressure freezing. After subsequent freeze-substitution and embedding in plastic resin, the cells of interest were relocated, sectioned and imaged by transmission EM (Figure 1A). Using this workflow, we could study the ultrastructure of cells and their organelles at precisely-

defined cell cycle stages. In this study, we focused on three timepoints: late anaphase (4-6 min after anaphase onset), telophase (8-10 min after anaphase onset), and interphase (Figure 1A).

To identify ER-NE junctions in EM samples, we first acquired tomograms covering the entire NE at a high speed and with sufficient magnification to resolve ER from NE membranes ("quick tomograms", see Methods). From these quick tomograms, we identified regions where the ER and NE were in close proximity and acquired high-quality tomograms (Figure 1B, see Methods). The high-quality tomograms allowed the identification of ER-NE junctions, where the lipid bilayer of the ER membrane is continuous with the ONM of the NE (Figure 1C), and provided the 3D ultrastructure of ER-NE junctions (Figure 1D, Supplementary movie 1).

ER-NE junctions are narrow and constricted in interphase

We first characterized the ultrastructure of ER-NE junctions in interphase. High-quality tomograms revealed distinct types of ER-NE junctions: (i) those with a lumen (i.e. the ER/NE lumen is clearly visible at the interface) and (ii) those without a lumen (i.e. the ER/NE lumen is not visible at the interface, despite the continuous membrane of the ER and the ONM) (Figure 2A, Supplementary Figure 1). To investigate the morphology of the ER-NE junctions, we segmented the ER/NE membranes in tomographic slices and generated 3D meshes of ER-NE junctions (Figure 2B, Supplementary Figure 1). Based on the 3D meshes, we drew membrane profiles across the centre of the lipid bilayers at the sagittal (side view) and transversal (top view) planes (Figure 2A, C). The membrane profile analysis revealed that ER-NE junctions form a constricted shape (Figure 2D). The cross-sectional width of the constricted region ranged from 6 to 22 nm (Figures 2D, 3H). No ER-NE junctions larger than 22 nm were identified in any of the seven cells in

interphase that we analysed. In short, our ultrastructural analysis demonstrated that ER-NE junctions form an “hourglass” shape with a constriction of 13.6 ± 5.3 nm wide at the interface between the ER and the NE.

Next, we asked if the constricted morphology is unique to ER-NE junctions or common for junctions within the ER. Returning to the same interphase cells, we selected ER-ER junctions consisting of an ER tubule fused perpendicularly to an ER sheet, which are topologically similar to ER-NE junctions, and analysed their 3D morphology (Figure 2E, F). In clear contrast to ER-NE junctions, ER-ER junctions had no membrane constrictions (Figure 2E) and they were mostly characterized by a wide triangle-shaped base at the junction interface (Figure 2E-G). The cross-sectional area of ER-ER junctions was considerably bigger than that of ER-NE junctions (Figures 2D, G, 3H). Altogether, our ultrastructural analysis of interphase cells showed that ER-NE junctions form a constricted hourglass shape that is distinct from the broad ER-ER junctions.

ER-NE junctions become constricted in telophase

In metazoan cells that undergo open mitosis, the NE breaks down at mitotic onset and it reforms again from membranes of the ER (Ungricht & Kutay, 2017). We thus investigated the ultrastructure of ER-NE junctions when the NE is first established during mitotic exit. Using the correlative microscopy assay (Figure 1A), we selected cells at late anaphase (4 to 6 minutes after the onset of anaphase) for EM observation (n=3 cells). In these cells, we found ER contacting small regions at the surface of chromatin, but the NE was still indistinguishable from the ER (Figure 3A, B). The junctions at the precursor ER/NE membranes (Figure 3C) were not constricted and had a similar morphology to junctions within the ER in interphase (Figure 2E), indicating that nascent ER-NE junctions in late anaphase have not adopted their specialized constricted morphology yet.

We then studied cells at early telophase (8 to 10 minutes after the onset of anaphase, n=2 cells) (Figure 3D). At this stage, the NE is clearly distinct from the ER as it covers the nucleus of the daughter cells almost completely (Figure 3D, E). The 3D ultrastructural analysis revealed that ER-NE junctions in telophase exhibit mixed morphologies; i.e. some are constricted at the ER/NE interface similar to the ER-NE junctions in interphase, while others are not constricted, and similar to junctions within the ER (Figure 3F-H). The average cross-section width was 26.2 ± 7.9 nm (Figure 3H), which is in between that of ER-NE junctions and the junctions within the ER in interphase (Figure 3H). These data suggest that the constriction of ER-NE junctions already starts at early telophase.

The constricted morphology of ER-NE junctions is observed in different mammalian cells

To determine if the constricted morphology of ER-NE junctions in interphase is specific to HeLa cells or a general feature of mammalian cells, we used publicly available whole cell EM datasets. We quantified ER-NE and ER-ER junctions in HeLa, human macrophage, and mouse pancreatic islet cells available on OpenOrganelle (Heinrich et al., 2021; Xu et al., 2021) (Figure 4A-F). In these datasets, entire cells were imaged by focused ion beam scanning EM (FIB-SEM) at a voxel size of around 4 nm (Figure 4A). While the spatial resolution is ten times lower than our EM tomography (Figures 1-3), we found that it was sufficient to identify and quantify the width of potential ER-NE junctions (Figure 4B-F). To study ER-NE junctions in an unbiased manner, we took a stereology-based approach. The regions of interest were uniformly sampled on the entire nuclear surface within a 1 μm radius sphere, and those regions were inspected for potential ER-NE junctions (Figure 4A). The width of ER-NE junctions in the HeLa, macrophage, and pancreatic islet cells were approximately 23, 20 and 26 nm (Figure 4E,

F), respectively, consistent with the constricted widths that we measured in our high-quality EM tomograms (Fig. 2D). In contrast, the ER-ER junctions were wider than the ER-NE junctions from the same cells (Figure 4B-F; Supplementary Figure 2). In the mouse pancreatic islet cell, 32 out of the 34 junctions quantified were constricted; only 2 junctions had widths above 100 nm (Figure 4D, F). Due to the lower spatial resolution of the FIB-SEM data, the ER-NE junctions that we analysed here may contain false positives, namely, ER membranes that are in proximity to, but not fused with the outer nuclear membrane (see Supplementary Figure 2). Nevertheless, we rarely found ER-NE junctions that were not constricted. The analysis of FIB-SEM images confirm the morphological traits that distinguish ER-NE from ER-ER junctions in our EM tomograms (Figure 2), and extend our findings to different mammalian cells.

ER-NE junctions are not constricted in yeast

ER-NE junctions with an hourglass-shaped morphology has not been observed in yeast (Friedman and Voeltz, 2011). To confirm this observation and ask if the hourglass-shaped morphology is conserved among eukaryotes, we visualised ER-NE junctions in high-pressure frozen yeast by EM tomography (Figure 4G). In agreement with the previous study (Friedman and Voeltz, 2011), cisternal and tubular ER forms junctions with the NE (Figure 4G). Most ER-NE junctions exhibited a wide triangle-shaped base at the junction interface with no apparent membrane constrictions. The quantification of the junction widths showed that ER-NE junctions in yeast are variable (Figure 4H). Therefore, we conclude that the hourglass-shaped morphology of ER-NE junctions is conserved in mammalian cells, but not in yeast.

DISCUSSION

While inter-organelle communication has emerged as a frontier in cell biology, the structure and physiological role of the junctions connecting the ER to the NE remain poorly understood. Our study used correlative light-electron microscopy to uncover the native ultrastructure of ER-NE junctions in high-pressure frozen mammalian cells for the first time. In interphase cells, we discovered that the ER forms hourglass-shaped, constricted and narrow (~15 nm in diameter) junctions to the NE that are clearly distinct from the broad junctions within the ER. While the constricted morphology of ER-NE junctions has previously been reported for high-pressure frozen plant cells (Craig and Staehelin, 1988), this has not been reported for yeast (Friedman and Voeltz, 2011; Figure 4) or Clamydomonas (see a cryo-EM tomogram published by Albert et al., 2017). Therefore, the constricted morphology of ER-NE junctions that we discovered in mammalian cells seems conserved only among higher eukaryotes. We also revealed that, when the ER-NE junctions are newly built during NE assembly at late anaphase, their morphology resembles the ER-ER junctions. In contrast, ER-NE junctions are already partially constricted in early telophase cells, indicating that their constricted shape is rapidly formed after mitosis and presumably maintained for the rest of the cell cycle (Figure 5A). Below we discuss a series of structural and functional implications derived from this intriguing finding.

Molecular mechanism underlying the morphology and biogenesis of ER-NE junctions

For maintaining the constricted shape of ER-NE junctions, membrane remodelling proteins are expected at the junction neck to counteract membrane tension of the ER/NE (Figure 5B). It is possible that proteins forming and stabilizing junctions in the ER,

including Atlastins and Lunapark (Wang et al., 2016; Pawar et al., 2017), are involved in regulating the specialized morphology of ER-NE junctions. However, an additional set of proteins is presumably required to differentially remodel the ER-NE junctions from ER-ER junctions. We discovered that the ER-NE junctions become constricted at telophase, which leads us to speculate that proteins responsible for remodelling ER-NE junctions might start to be specifically recruited to the NE in early telophase. It is also likely that the regulatory proteins are predominantly or exclusively expressed in higher eukaryotes. Future studies combining high-resolution imaging with molecular perturbation assays will be required to identify the molecular players responsible for shaping and stabilizing ER-NE junctions.

The biogenesis of ER-NE junctions is an important question that must be addressed, considering the dynamic remodelling of ER and nucleus (Nixon-Abell et al., 2016; Ungricht & Kutay, 2017). We envision that ER-NE junctions are likely generated *de novo* during interphase. In one scenario, the NE may extend membrane protrusions, but we did not observe any examples in our EM images apart from budding vesicles. We thus favor the scenario where ER-NE junctions are generated from ER tubules that contact and eventually fuse with the NE. There were many ER tubules whose membrane was juxtaposed (but not fused) to the ONM (Supplementary Figure 1), as well as extremely constricted junctions where the ER membrane seemed fused to the ONM without having a luminal space (Figure 2). We speculate that these structures are assembly intermediates, and that certain proteins have to be recruited to those contact sites for mediating membrane fusion and/or dilation of the junctions. Considering the large number of these assembly intermediates, the fusion and dilation events may be a rate-limiting step for the formation of new junctions. These morphological traits support the presence of a still unknown mechanism that restricts the formation and size of ER-NE junctions.

Functional implications of the constricted morphology of ER-NE junctions

The constricted ultrastructure of ER-NE junctions may allow them to act as a selective barrier for the transport of lipids, large protein complexes, and protein aggregates between the ER and the NE (Figure 5B). A previous study showed that phosphatidylserine (one of the major acidic phospholipids in eukaryotic cells) is enriched on the ER membrane compared to the outer nuclear membrane despite their continuity (Tsuji et al., 2019). Since phosphatidylserine is a cylindrical-shaped lipid that favours the formation of flat membranes (Peeters et al., 2022), ER-NE junctions with highly-curved membranes may limit phosphatidylserine diffusion. As NE lipid composition affects NE protein stability (Lee et al., 2022), ER-NE junctions may function as selective lipid sorter and play a key role in NE protein homeostasis as proposed previously (Bahmanyar & Schlieker, 2020).

We found that the average width of ER-NE junctions is 15 nm, which is larger than the 5 nm size of typical proteins, but small enough to potentially restrict the diffusion of large multimeric protein complexes and aggregates. Interestingly, Apomucin, which forms large protein oligomers of 500 to 1000 kDa (Eckhard et al., 1987), has been found to localise predominantly in the ER lumen rather than the NE lumen in mammalian cells (Deschuyteneer et al., 1988). We speculate that ER-NE junctions prevent the NE entry of such large protein complexes, and perhaps also misfolded proteins that are prone to form large aggregates in the ER lumen (Sun & Brodsky, 2019). In this way, the constricted junctions may limit the entry of toxic molecules into the NE.

It should also be noted that there are two types of ER-NE junctions: with and without a clear luminal connection (Figure 2A-C). This raises a possibility that ER-NE junctions can switch their configuration. The membrane contact sites between the ER and other organelles such as mitochondria, endosome, and plasma membrane have been shown to

respond to various environmental cues including nutrient stress, ER stress and calcium stimulation (Donahue et al., 2022; Jang et al., 2022). Similarly, the membrane junctions between the ER and the NE might change their morphology in response to environmental stimuli. It would be interesting to examine the dynamic nature of the junctions under physiological stresses.

Physiological and pathological relevance of ER-NE junctions

The NE proteins supplied via ER-NE junctions have critical roles in gene expression, nuclear organization, and nuclear pore biogenesis, as well as in development and disease (Gauthier and Comaills, 2021). ER-NE junctions are envisioned to contribute to these key nuclear functions, in addition to their potential functions as a selective sorter of proteins and lipids discussed above. Dysregulated nuclear size, mislocalised NE proteins, and dysfunction of ER-shaping proteins have been associated with many diseases including cancer and neurodegenerative disorders (Jevtic and Levy, 2014; Öztürk et al., 2020; Rose et al., 2022). However, few physiological processes have been linked to ER-NE junctions, possibly due to the lack of studies focusing on this particular type of junction. Our finding that ER-NE junctions adopt a specialised constricted morphology provides the basis for future studies of their molecular mechanism and functions under physiological and pathological conditions.

FIGURE 1

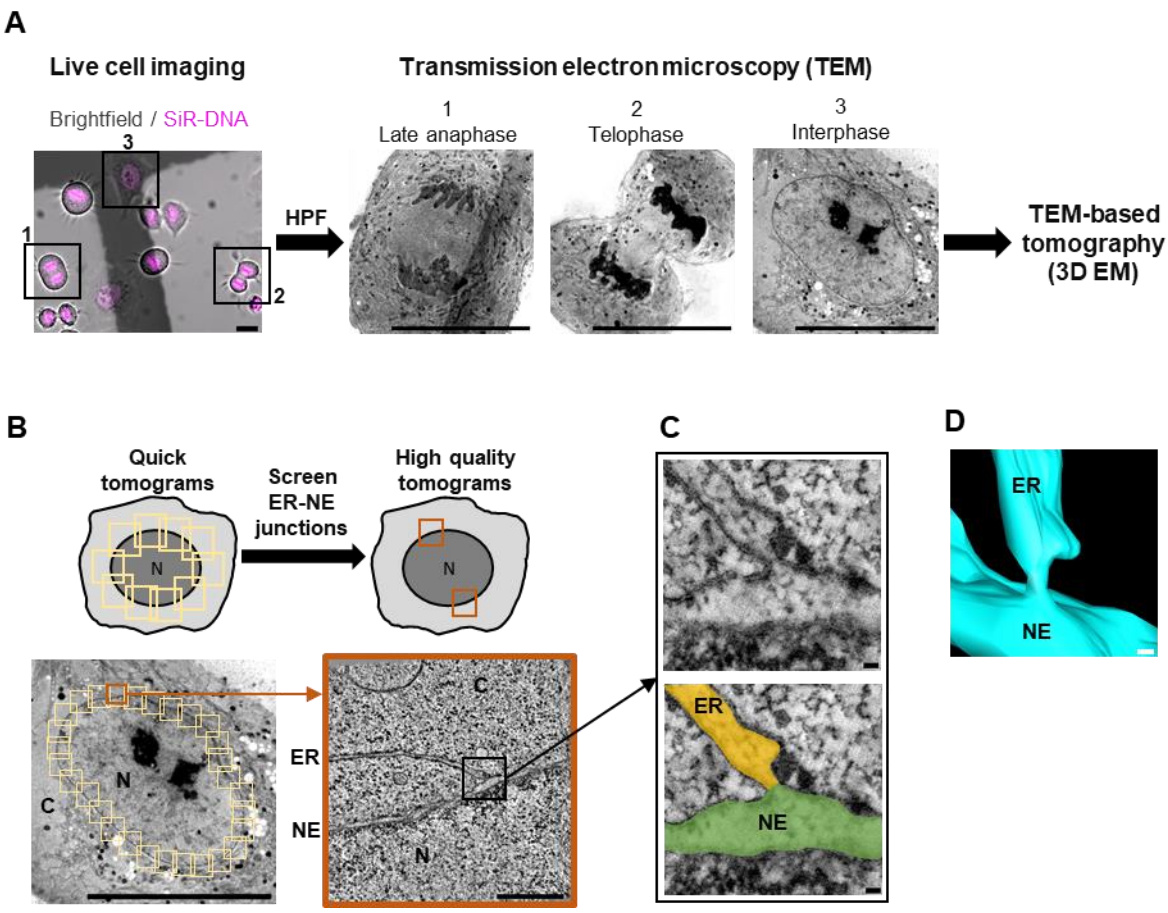

Figure 1. Method to systematically study the 3D ultrastructure of ER-NE junctions along the cell cycle. A, Correlative live cell imaging with electron microscopy to image the same cells using both imaging modalities. Cell-cycle progression of HeLa cells was monitored by live cell imaging in the bright-field and far-red (SiR-DNA) channels. Cells were high-pressure frozen (HPF) in late anaphase, telophase or interphase, and relocated under a transmission electron microscope (TEM) for tomography. Scale bars: 20 µm. **B,** Tomography-based screen to search for ER-NE junctions around the NE in an untargeted manner. Tomograms covering the entire NE were acquired quickly and then, high quality tomograms were taken at regions with potential ER-NE junctions. Scale bars: 20 µm (overview), 500 nm (inset). **C,** An electron tomographic slice of an ER-NE junction. The membrane of the ER and the outer nuclear membrane are clearly visible in the high quality tomogram. Scale bar: 20 nm. **D,** 3D mesh of the ER-NE junction shown in **C**. Scale bar: 20 nm. ER: endoplasmic reticulum, NE: nuclear envelope C: cytoplasm, N: nucleus.

FIGURE 2

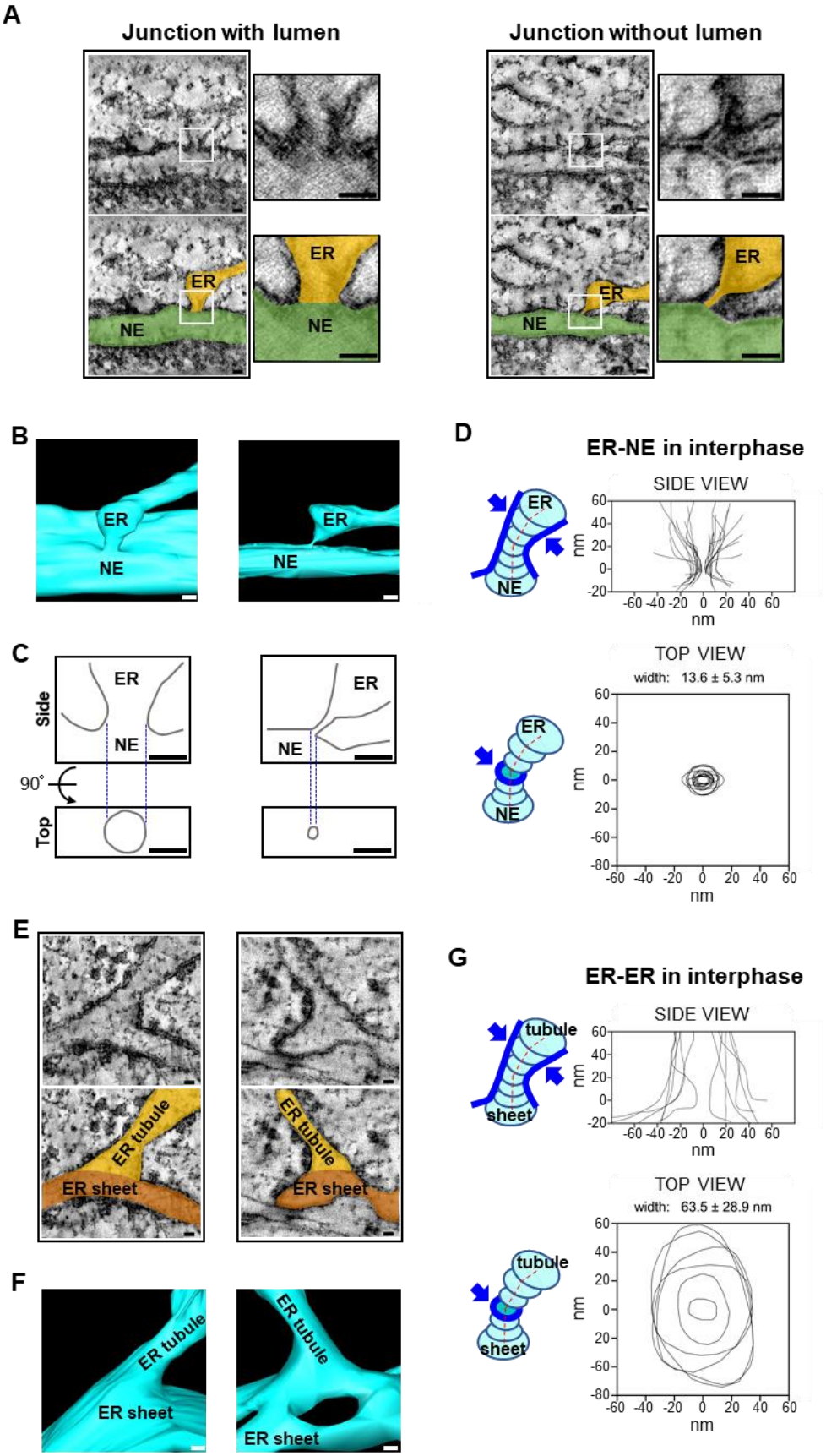
A
Junction with lumen
Junction without lumen
ER
NE
B
C
Side
Top
90°
D
ER-NE in interphase
SIDE VIEW
TOP VIEW
width: 13.6 ± 5.3 nm
nm
E
ER tubule
ER sheet
F
G
ER-ER in interphase
tubule
sheet
width: 63.5 ± 28.9 nm

Figure 2. The membranous junctions that link the ER to the NE in interphase are narrow, constricted, and distinct from the junctions within the ER. A, Electron tomographic slices of ER-NE junctions with and without a lumen at their sagittal planes. For each junction, an enlargement of the region containing the junction is displayed. The top row shows raw EM data; the bottom row, the EM data on which the ER and the NE are colored in orange or green, respectively. **B,** 3D meshes of the ER-NE junctions shown in **A**. **C,** Membrane profiles of the side and top views of the junctions shown in **A**. **D,** Plots overlaying membrane profiles of the side and top views of ER-NE junctions found in interphase cells. n = 14 junctions from 4 cells. **E,** Electron tomographic slices of ER-ER junctions (in which an ER tubule is fused perpendicularly to an ER sheet) at their sagittal planes. The top row shows raw EM data; the bottom row, the EM data on which an ER tubule and an ER sheet are colored in orange or brown, respectively. **F,** 3D meshes of the ER tubule-sheet junctions shown in **E**. **G,** Plots overlaying the side and top views of the ER tubule-sheet junctions found in interphase cells. n = 6 junctions from 4 cells. Scale bars for **A-C, E, F**: 20 nm.

FIGURE 3

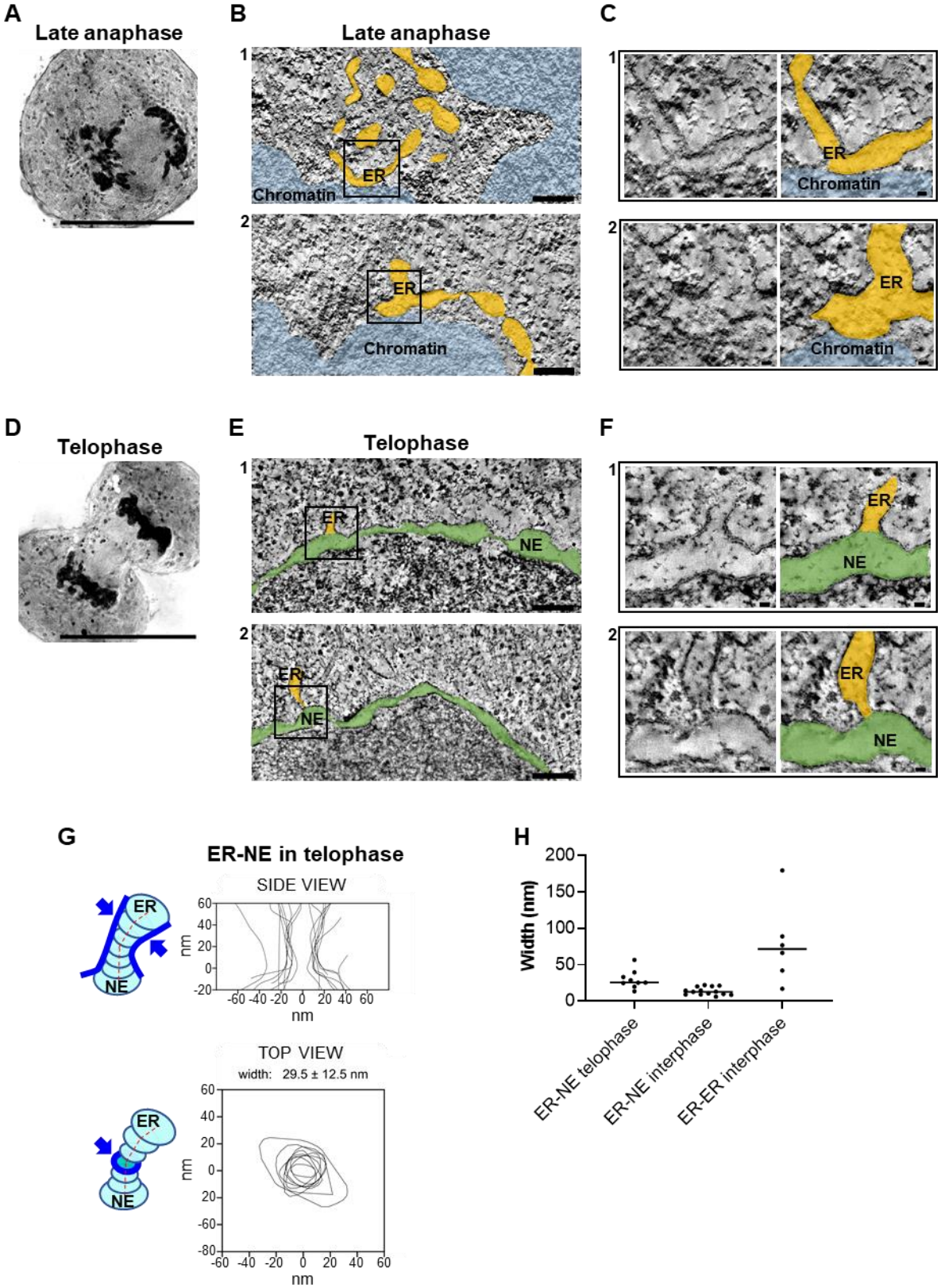

Figure 3. ER-NE junctions get progressively constricted during mitotic exit. A, 2D EM micrograph of a cell in late anaphase. **B,** Tomographic slices of cells in late anaphase showing that the ER (orange) starts to contact the chromatin (blue), but the NE is still

indistinguishable. **C,** Enlargement of the regions indicated in **B**. For each junction, the left image shows raw EM data; the right one, the EM data on which the ER and the chromatin are colored in orange or blue, respectively. **D,** 2D EM micrograph of a cell in telophase. **E,** Tomographic slices showing that the NE is established in telophase and ER-NE junctions are present. **F,** Enlargement of the regions indicated in **E**. For each junction, the left image shows raw EM data; the right one, the EM data on which the ER and the NE are colored in orange or green, respectively. **G,** Plots overlaying the side and top views of the ER-NE junctions found in telophase cells. n = 9 junctions from 2 cells. **H,** The cross-section width of the constricted neck of ER-NE junctions in telophase and interphase, as well as the width of ER tubule-sheet junctions. n = 9, 14, and 6 for ER-NE telophase, ER-NE interphase, and ER-ER interphase. Scale bars for **A, D**: 20 μm; Scale bars for **B, E**: 200 nm; Scale bars for **C, F**: 20 nm.

FIGURE 4

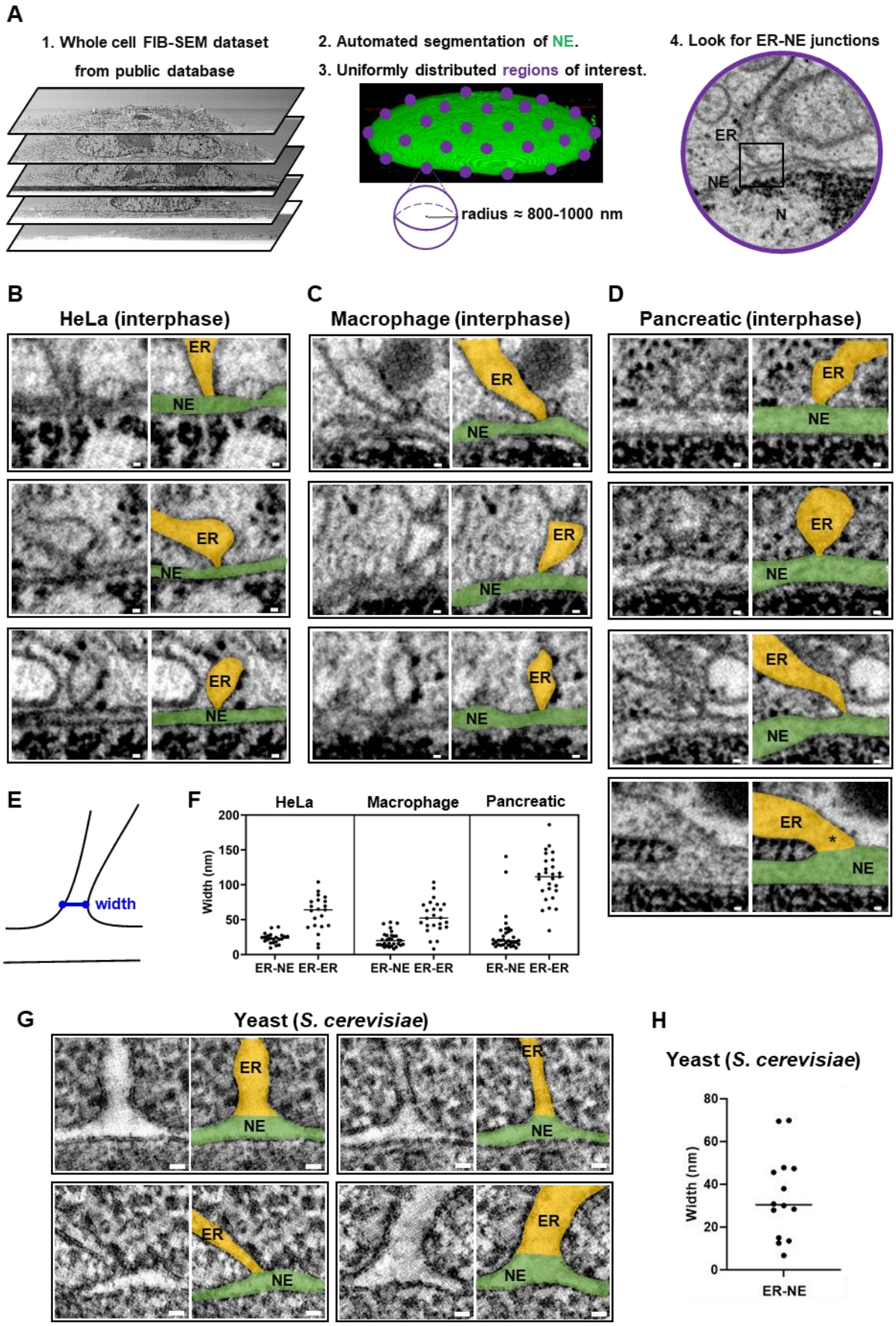
A
1. Whole cell FIB-SEM dataset
from public database
2. Automated segmentation of NE.
3. Uniformly distributed regions of interest.
radius ≈ 800-1000 nm
4. Look for ER-NE junctions
ER
NE
N
B
HeLa (interphase)
C
Macrophage (interphase)
D
Pancreatic (interphase)
E
width
F
HeLa
Macrophage
Pancreatic
Width (nm)
200
150
100
50
0
ER-NE ER-ER
ER-NE ER-ER
ER-NE ER-ER
G
Yeast (S. cerevisiae)
H
Yeast (S. cerevisiae)
Width (nm)
80
60
40
20
0
ER-NE

Figure 4. ER-NE junctions are constricted in several mammalian cell lines, but not in yeast. A, Stereology-based approach to find ER-NE junctions in FIB-SEM datasets of entire cells. The datasets were downloaded from OpenOrganelle (Heinrich et al., 2021; Xu et al., 2021). On the surface of automatically-segmented nuclei, the regions of interest were uniformly sampled with a radius of 800-1000 nm. In these regions, potential ER-NE junctions were searched manually. **B-D,** ER-NE junctions in raw FIB-SEM images of a HeLa cell (**B**), a human macrophage (**C**), and a mouse pancreatic islet cell (pancreatic) (**D**). For each junction, the left image shows raw EM data; the right one, the EM data on which the ER and the NE are colored in orange or green, respectively. The asterisk indicates one of the two junctions with a width above 100 nm. **E,** A scheme depicting how the width of junctions was measured using a 2-point line (blue). **F,** Widths of ER-NE and ER-ER junctions in a HeLa cell, a macrophage and a mouse pancreatic islet cell. n = 23 ER-NE and 21 ER-ER junctions for a HeLa cell, n = 31 ER-NE and 24 ER-ER junctions for a macrophage, and n = 34 ER-NE and 27 ER-ER junctions for a mouse pancreatic islet cell. **G,** Tomographic slices of ER-NE junctions of yeast (*Saccharomyces cerevisiae*) cells at their sagittal planes. **H,** Widths of ER-NE junctions measured in yeast cells. n = 14 junctions from 8 cells. Scale bars for **B-D, G**: 20 nm.

FIGURE 5

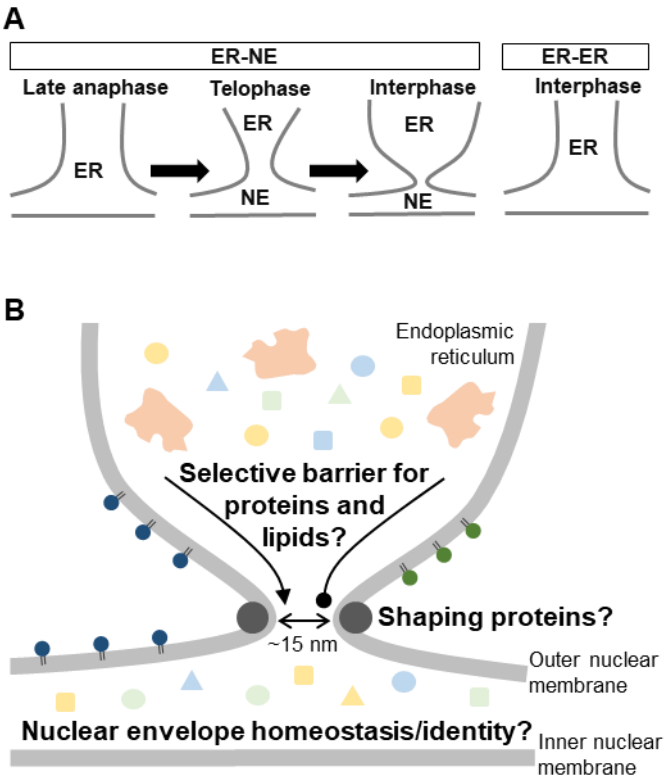

Figure 5. Model for the formation and function of ER-NE junctions in higher eukaryotes. A, ER-NE junctions are progressively specialized after telophase, and form a constricted hourglass-shaped morphology that is distinct from the broad junctions within the ER. **B,** Implications and potential functions associated with the tight morphology of ER-NE junctions in interphase.

METHODS

Cell culture

Wild-type HeLa Kyoto cells (RRID:CVCL_1922) were incubated in Dulbecco's Modified Eagle Media (DMEM with low glucose, Sigma, D6046-500ML) supplemented with 10% fetal calf serum (FCS, Sigma, F7524-500ML) and 1% Penicillin-Streptomycin (Pen/Strep, Sigma, P4333-100ML). Cells tested negative for mycoplasma infection using a mycoplasma detection kit (Biological Industries, 20-700-20).

Cell seeding and cell cycle synchronization for correlative light and electron microscopy

Carbon-coated sapphire discs (D6mm, Leica Microsystems) were assembled on 1-well cups for SampLink chambers (Leica Microsystems). The assembled SamplLink chambers were washed in 70% ethanol, exposed to UV light for 20-30 minutes, and dried overnight. Before seeding the HeLa cells, the sapphire discs were coated with 0.1 mg/ml poly-L-lysine hydrobromide (Sigma, P1274) for 1-1.5 hours at 37°C. Few hours after seeding the cells, when most cells had adhered to the sapphire disc, the media was replaced with 2 mM thymidine (Sigma, T9250-1G) in DMEM+10%FCS+Pen/Strep media overnight. On the next day, samples were washed twice in Dulbecco's Phosphate Buffered saline (DPBS, Sigma, D8537) and incubated in fresh DMEM+10%FCS+Pen/Strep media to release cells from the first thymidine block. Six hours later, samples were washed in PBS and incubated in 2mM thymidine in DMEM+10%FCS+Pen/Strep overnight. On the following day, samples were washed twice in PBS and incubated in fresh DMEM+10%FCS+Pen/Strep media to release cells from the second thymidine block.

Live cell imaging and high-pressure freezing

Eight hours after the release from the second thymidine block, the media was replaced with imaging media (DMEM without phenol red, Genaxxon) containing SiR-DNA (Spirochrome, SC007) 1:2000 to label DNA. An hour later, samples were transported to the light microscope using the Baker Ruskinn OxyGenie transportable incubator (Leica Microsystems) at 37°C equipped with gas cylinders (Catalina Cylinders) filled with 5% CO_2 in a synthetic atmosphere of 20%O_2 and 80% N_2. Cells in the SampLink chambers were monitored in the light microscope THUNDER Imager Nano (Leica Microsystems) coupled with an incubator at 37°C. Time-lapses of regions enriched in metaphase cells were acquired every 20 seconds in the bright-field and far-red (SiR-DNA) channels using a 20x/0.40DRY NPLAN Epi objective (Leica Microsystems). When most dividing cells in the field of view reached late anaphase and telophase, samples were high-pressure frozen within 1 to 1.5 minutes using the High Pressure Freezer Leica EM ICE equipped with the Coral Life workflow (Leica Microsystems). Cells were frozen in DMEM+10%FCS+Pen/Strep supplemented with 20% FICOL-PM400 (Sigma, F4375-25G) as a cryoprotectant, which was added to the samples few seconds before freezing. The lid carriers (Leica Microsystems) had a cavity depth of ~25 µm, and they had been in contact with 1-hexadecene (Merck, 8.22061.0100). After high-pressure freezing, sapphire discs were stored in liquid nitrogen until the subsequent sample preparation steps.

Freeze substitution and resin embedding

Freeze substitution was performed as described previously (Bragulat-Teixidor et al., 2022). Briefly, samples were transferred in a Leica EM AFS-2 freeze substitution unit (Leica Microsystems). The samples were substituted in 0.1% uranyl acetate (UA), 2%

Osmium tetroxide (Electron Microscopy Sciences, 19134) and 5% H_2O in acetone (PanReac AppliChem, ITW reagents, 141007.1211) following this temperature ramp: -90°C to -80°C for 10 hours, -80°C to -30°C for 10 hours, -30°C for 4 hours, -30°C to 0°C for 6 hours, 0°C to 20°C for 4 hours, 20°C for 5-6 hours. Afterwards, samples were washed three times in pure acetone for at least 10 minutes each, and subsequently infiltrated with Agar 100 Epoxy resin (Agar Scientific). The resin infiltration was done progressively at room temperature with increasing concentrations of resin in acetone (3:1 for 2-3 hours, 1:1 for 2-3 hours, and 1:3 overnight). Infiltration with pure resin was done at room temperature for at least 5 hours. Resin was polymerized at 60°C for 72 hours.

Sectioning, gold bead attachment and post-staining

Resin blocks were sectioned every 250 nm using a Diamond knife (Diatome) and an ultramicrotome Leica ultracut UCT (Leica Microsystems). Sections were collected on Cu/Pd slot grids (Agar Scientific, G2564PD) coated with a film of 1% formvar (Agar Scientific) in chloroform (Sigma Aldrich, 32211-1L-M). To allow better alignment of dual axis tomography, 15-nm gold beads conjugated with Protein A (Cytodiagnostics, AC-15-05-10) were attached to both sides of the grids. To enhance membrane contrast, sections were post-stained at room temperature with 2% uranyl acetate in 70% methanol for 10 minutes and with Reynold's lead citrate 3% (Delta Microscopies) for 7 minutes.

Electron tomography

As ER-NE junctions are too tiny to be identified reliably on 2D micrographs, we developed a two-step tomography-based screen consisting of "quick" and "high quality" tomograms. The first step aimed at minimizing the acquisition time of the tilt series while allowing sufficient image quality to resolve ER from NE membranes. These tilt series

were acquired over a ± 20º tilt range with an angular increment of 2º at a pixel size of 0.567 nm. These tomograms were taken with slight overlaps to cover the entire NE in one or more sections per cell (Figure 1B). These tilt series allowed the reconstruction of "quick" tomograms, which were screened manually for potential ER-NE junctions. In the second step of the screen, "high quality" tomograms (typically dual axis, from tilt series with a ± 50º tilt range, an angular increment of 1º, and a pixel size of 0.451 nm) were taken at the regions where the "quick" tomograms revealed potential ER-NE junctions.

Similarly to ER-NE junctions, we established a two-step tomography-based screen to search for ER-ER junctions with a similar topology to ER-NE junctions (i.e. an ER tubule contacting perpendicularly to an ER sheet) in the same cells where ER-NE junctions were analysed. The screen consisted of "low magnification" tomograms (from tilt series with a ± 50º tilt range, an angular increment of 1º, and a pixel size of 1.137 and 2.181 nm) and "high quality" tomograms (typically dual axis, from tilt series with a ± 50º tilt range, an angular increment of 1º, and a pixel size of 0.451 nm). The "low magnification" tomograms allowed to find ER-ER junctions in the cytoplasm; the "high quality" tomograms, to image the junctions at a high magnification for a better visualization and quantification. The tomograms were reconstructed from tilt series with the R-weighted backprojection method implemented in the IMOD software package (version 4.11.7) (Kremer et al., 1996). The tilt series were acquired using the Serial EM software (v3.x) under the transmission electron microscope (TEM) Tecnai G2 20 operated at 200 kV and equipped with an Eagle 4k HS CCD camera. The Stitching plugin (Preibisch et al., 2009) in FIJI (Schindelin et al., 2012) was used to efficiently relocate the tomograms in stitched overviews of the cells.

Electron microscopy of yeast cells

Wild-type strains of yeast (*Saccharomyces cerevisiae*, BY4741, Euroscarf) cells were cultured at 30ºC in synthetic dextrose complete media. Cells were high-pressure frozen at the log phase and freeze substituted as described previously (Romanauska and Köhler, 2021). Sections with a thickness of 400 nm were cut using a Leica UCT ultramicrotome (Leica Microsystems). The grids were coated with 15-nm gold beads conjugated with Protein A on both sides, and the sections were post-stained with 2% UA in methanol and Reynold's lead citrate as described above. Cells were observed using the Serial EM software (v3.x) under the transmission electron microscope (TEM) Tecnai G2 20 operated at 200 kV and equipped with an Eagle 4k HS CCD camera. At the regions where ER was visible near the NE, dual axis tomograms were acquired typically over a -60° to +60° tilt range with an angular increment of 1° at a pixel size of 0.451 nm.

Mesh generation

Meshes of the junctions were generated using the IMOD software after manually tracing the ER membrane, ONM and INM across the middle of their lipid bilayer every 4.51 nm tomographic slices.

Side and top profiles of ER-NE and ER-ER connections in tomograms

Based on the 3D mesh, we identified the sagittal and transversal planes that cut the junctions for the side or the top views, respectively. The side profiles were drawn by tracing manually the ER membrane and the ONM across the middle of the lipid bilayer after rotating the EM tomogram to the orientation of the sagittal plane in the Slicer mode of IMOD. The top profiles were drawn manually across the middle of the lipid bilayer at the neck of the junction after orienting the EM tomograms in the Slicer mode of IMOD

(Kremer et al., 1996; version 4.11.7). The width of junctions was defined as the average of the longest and shortest lengths of the bounding rectangle around the top view profiles.

Stereology-based approach to look for ER-NE junctions in FIB-SEM datasets

We developed a stereology-based approach to search for ER-NE junctions in FIB-SEM datasets. We downloaded the datasets of a HeLa cell (jrc_hela-2; voxel size (nm) of 4.0 x 4.0 x 5.2 in x, y, z), a human macrophage (jrc_macrophage-2; voxel size (nm) of 4.0 x 4.0 x 3.4 in x, y, z), and a mouse pancreatic islet cell treated with high glucose (jrc_mus-pancreas-1; voxel size (nm) of 4.0 x 4.0 x 3.4 in x, y, z) from OpenOrganelle (Heinrich et al., 2021; Xu et al., 2021). To identify the NE in the FIB-SEM datasets, segmentations of the entire nucleus were required. The segmentations of the nuclei of the HeLa and the macrophage cells were available on OpenOrganelle. For the mouse pancreatic islet cell, we segmented the nucleus automatically doing a pixel classification in Ilastik (Stuart et al., 2019; version 1.3). The automated segmentations were refined using filters and other options for binary images in FIJI so that the surface of the automatically-segmented nuclei would coincide with the NE on the raw data. For each nuclei, ~50 points were selected at the surface of the automatically-segmented nuclei using a custom-written script. The first point was selected randomly, and the rest of points were distributed uniformly at the NE in a radial way from the randomly-positioned first point. Around each point, spherical regions with a radium of ~800-1000 nm were screened manually to identify potential ER-NE junctions. To compare ER-NE with ER-ER junctions, three-way junctions were searched in the ER at random regions of cytoplasm.

Quantification of width of ER-NE and ER-ER junctions in FIB-SEM datasets and in yeast tomograms

The widths were quantified in IMOD. For constricted junctions, the width corresponded to the length of a 2-point line traced across the neck of the junction at the sagittal plane. For non-constricted junctions, the width was measured with a 2-point line across the middle of the triangulated base of the junction at the sagittal plane. The widths of ER-NE junctions identified in yeast tomograms were quantified in the same way as the junctions in the FIB-SEM datasets.

ACKNOWLEDGEMENTS

This project was supported by laboratory startup funding from Medical University of Vienna to S.O. and by the Vienna Science and Technology Fund (WWTF; project LS19-001) to S.O.. H.B.T. received a DOC Fellowship of the Austrian Academy of Sciences (no. 25951) and a Max Perutz PhD Fellowship (University of Vienna and the Medical University of Vienna). The authors acknowledge the Electron Microscopy facilities at the Vienna BioCenter and EMBL Heidelberg (especially Martin Schorb and Paolo Ronchi) for technical support and discussion. In addition, we thank Paul Würzinger and Robert Kirmse (LEICA Microsystems) for technical support. The yeast samples for EM were kindly provided by Annette Romanauska (Alwin Köhler's lab). The authors acknowledge the members of the labs of Shotaro Otsuka (especially Tamara Völkerer, Julia Scholz, Kaike Ren, Pauline Vinet, and Nikoleta Kavaja), Alwin Köhler, Elif Karagöz, Roland Foisner and David Haselbach for feedback and discussions. Eija Jokitalo also provided us with valuable references.

AUTHOR CONTRIBUTIONS

H.B.T. and S.O. conceived the project with input from K.I.. H.B.T. performed all the electron microscopy experiments and analyses. H.B.T. and K.I. established a computational image analysis pipeline to quantify ultrastructures in 3D. G.M.S. supported EM image analysis. S.O. supervised the work. H.B.T., K.I. and S.O. wrote the paper. All authors contributed to the analysis and interpretation of data.

REFERENCES

Albert S, Schaffer M, Beck F, Mosalaganti S, Asano S, Thomas HF, Plitzko JM, Beck M, Baumeister W, Engel BD. Proteasomes tether to two distinct sites at the nuclear pore complex. Proc. Natl. Acad. Sci. U. S. A., 114(52):13726–13731 (2017).

Bahmanyar S, Schlieker C. Lipid and protein dynamics that shape nuclear envelope identity. Mol. Biol. Cell., 31(13):1315–1323 (2020).

Bragulat-Teixidor H, Hossain MJ, Otsuka S. "Visualizing Nuclear Pore Complex Assembly In Situ in Human Cells at Nanometer Resolution by Correlating Live Imaging with Electron Microscopy." Methods Mol. Biol., 2502:493–512 (2022).

Craig S and Staehelin LA. High pressure freezing of intact plant tissues. Evaluation and characterization of novel features of the endoplasmic reticulum and associated membrane systems. Eur. J. Cell Biol., 46(1):81–93 (1988).

Deschuyteneer M, Eckhardt AE, Roth J, Hill RL. The subcellular localization of apomucin and nonreducing terminal N-acetylgalactosamine in porcine submaxillary glands. J. Biol. Chem., 263(5):2452–9 (1988).

Donahue EKF, Ruark EM, Burkewitz K. Fundamental roles for inter-organelle communication in aging. Biochem. Soc. Trans., 50(5):1389–1402 (2022).

Eckhardt AE, Timpte CS, Abernethy JL, Toumadje A, Johnson WC Jr, Hill RL. Structural properties of porcine submaxillary gland apomucin. J. Biol. Chem., 262(23):11339–44 (1987).

Friedman JR and Voeltz GK. The ER in 3D: a multifunctional dynamic membrane network. Trends. Cell Biol., 21(12):709–17 (2011).

Gauthier BR and Comaills V. Nuclear Envelope Integrity in Health and Disease: Consequences on Genome Instability and Inflammation. Int. J. Mol. Sci., 22(14):7281 (2021).

Heinrich L, Bennett D, Ackerman D, Park W, Bogovic J, Eckstein N, Petruncio A, Clements J, Pang S, Xu CS, Funke J, Korff W, Hess HF, Lippincott-Schwartz J, Saalfeld

S, Weigel AV; COSEM Project Team. Whole-cell organelle segmentation in volume electron microscopy. Nature, 599(7883):141–146 (2021).

Jang W, Puchkov D, Samsó P, Liang Y, Nadler-Holly M, Sigrist SJ, Kintscher U, Liu F, Mamchaoui K, Mouly V, Haucke V. Endosomal lipid signaling reshapes the endoplasmic reticulum to control mitochondrial function. Science, 378(6625):eabq5209 (2022).

Jevtic P and Levy DL. Mechanisms of nuclear size regulation in model systems and cancer. Adv. Exp. Med. Biol., 773:537–69 (2014).

Kremer JR, Mastronarde DN, McIntosh JR. Computer visualization of three-dimensional image data using IMOD. J. Struct. Biol. 116, 71–76 (1996).

Lee S, Merta H, Rodríguez JWC, Bahmanyar S, A membrane sensing mechanism couples local lipid metabolism to protein degradation at the inner nuclear membrane. bioRxiv. 2022.07.06.498903 (2022).

Nixon-Abell J, Obara CJ, Weigel AV, Li D, Legant WR, Xu CS, Pasolli HA, Harvey K, Hess HF, Betzig E, Blackstone C, Lippincott-Schwartz J. Increased spatiotemporal resolution reveals highly dynamic dense tubular matrices in the peripheral ER. Science, 354(6311) (2016).

Otsuka S, Bui KH, Schorb M, Hossain MJ, Politi AZ, Koch B, Eltsov M, Beck M, Ellenberg J. Nuclear pore assembly by an inside-out extrusion of the nuclear envelope. Elife, 5:e19071 (2016).

Öztürk Z, O'Kane CJ, Pérez-Moreno JJ. Axonal Endoplasmic Reticulum Dynamics and Its Roles in Neurodegeneration. Front. Neurosci., 14:48 (2020).

Pawar S, Ungricht R, Tiefenboeck P, Leroux JC, Kutay U. Efficient protein targeting to the inner nuclear membrane requires Atlastin-dependent maintenance of ER topology. Elife, 6:e28202 (2017).

Peeters BWA, Piët ACA, Fornerod M. Generating Membrane Curvature at the Nuclear Pore: A Lipid Point of View. Cells, 11(3):469 (2022).

Preibisch S, Saalfeld S, Tomancak P. Globally optimal stitching of tiled 3D microscopic image acquisitions. Bioinformatics, 25(11):1463–5 (2009).

Romanauska A, Köhler A. Reprogrammed lipid metabolism protects inner nuclear membrane against unsaturated fat. Dev Cell, 56(18):2562-2578.e3 (2021).

Rose M, Burgess JT, O'Byrne K, Richard DJ, Bolderson E. The role of inner nuclear membrane proteins in tumourigenesis and as potential targets for cancer therapy. Cancer Metastasis Rev., 41(4):953–963 (2022).

Rossini M, Pizzo P, Filadi R. Better to keep in touch: investigating inter-organelle cross-talk. FEBS J., 288(3):740–755 (2021).

Staehelin LA. The plant ER: a dynamic organelle composed of a large number of discrete functional domains. Plant J., 11(6):1151–65 (1997).

Sun Z and Brodsky JL. Protein quality control in the secretory pathway. J. Cell Biol., 218(10):3171–3187 (2019).

Tsuji T, Cheng J, Tatematsu T, Ebata A, Kamikawa H, Fujita A, Gyobu S, Segawa K, Arai H, Taguchi T, Nagata S, Fujimoto T. Predominant localization of phosphatidylserine at the cytoplasmic leaflet of the ER, and its TMEM16K-dependent redistribution. Proc. Natl. Acad. Sci. U. S. A., 116(27):13368–13373 (2019).

Ungricht R, Kutay U. Mechanisms and functions of nuclear envelope remodelling. Nat. Rev. Mol. Cell Biol., 18(4):229–245 (2017).

Wang S, Tukachinsky H, Romano FB, Rapoport TA. Cooperation of the ER-shaping proteins atlastin, lunapark, and reticulons to generate a tubular membrane network. Elife, 5:e18605 (2016).

Watson ML. The nuclear envelope; its structure and relation to cytoplasmic membranes. J. Biophys. Biochem. Cytol., 1(3):257–70 (1955).

Whaley WG, Mollenhauer HH, Leech JH, Some Observations on the Nuclear Envelope, J. Biophys. Biochem. Cytol., 8, 233–245 (1960).

Xu CS, Pang S, Shtengel G, Müller A, Ritter AT, Hoffman HK, Takemura SY, Lu Z, Pasolli HA, Iyer N, Chung J, Bennett D, Weigel AV, Freeman M, van Engelenburg SB, Walther TC, Farese RV Jr, Lippincott-Schwartz J, Mellman I, Solimena M, Hess HF. An open-access volume electron microscopy atlas of whole cells and tissues. Nature. 599(7883):147–151 (2021).